ICAS 2016 30th Congress of the International Council of the Aeronautical Sciences
DCC, Daejeon, Korea ; September 25-30, 2016

DESIGN AND DEVELOPMENT OF A MILITARY ENGINE INLET RESEARCH DUCT

R.P.M. Rademakers*, J.P. Haug*, R. Niehuis*, and M. Stößel**
*** Institute of Jet Propulsion, Universität der Bundeswehr München, Neubiberg, Germany**
**** Wehrtechnische Dienststelle für Luftfahrzeuge und Luftfahrtgerät der Bundeswehr, Manching, Germany**

Keywords: *military engine inlet research duct, engine test facility*

Abstract

The design and development of both the inlet and the propulsion system of military aircraft are often conducted separately. However, by using this approach the interactions of the aerodynamic conditions within both systems are not taken into account and hence an optimal inlet propulsion system cannot be conceived.

The requirements of modern military aircraft with a fully integrated propulsion system increase and thus research regarding inlet compressor interactions becomes more important in order to improve future systems. The Institute of Jet Propulsion hence decided to design and develop a military engine inlet system specifically for research purposes.

This paper first summarizes the initially defined goals and requirements within the current project. Computational Fluid Dynamics (CFD) simulations were conducted in order to assess the influence of certain geometrical shapes of an s-duct on the aerodynamic condition at the outlet plane of the inlet system. The gained knowledge was used during the design of a designated inlet geometry. Then, the necessary measurement instrumentation for this geometry in an experimental setup was defined with support from CFD simulations. Finally, all hardware including the duct for experimental testing in the institute's Engine Test Facility (ETF) in combination with a modified Larzac 04 C5 turbofan engine was developed and manufactured.

1. Introduction

The inlet and the propulsion system of military aircraft are often designed and developed as isolated systems since different sectors of the industry are responsible for the respective systems. In a late stadium of the development process both systems are merged for both full-aircraft ground testing and flight testing.

A similar approach is often used for general research within this field. In the open literature it can typically be distinguished between investigations on:

- the aerodynamics within serpentine inlet systems and
- the influence of distorted flow on a compressor system

The Institute of Jet Propulsion started research on "aerodynamics within serpentine inlet systems" with preliminary CFD simulations regarding the integration of bent inlet systems within the institute's ETF [1]. First experiments with the so-called generic s-duct geometry were conducted in a scaled version of this ETF by Rademakers et al. [2]. Brehm et al. [3] describe the aerodynamic transferability between both facilities by means of CFD. CFD simulations were moreover conducted to analyze varying flow conditions within an s-duct due to either different inflow conditions at the intake plane (Brehm et al. [4]) or different geometrical shapes of the s-duct itself (Kächele et al. [5], [6]).

Investigations regarding the "influence of distorted flow on a compressor system" started in the 1990s (see e.g. Schmid et al. [7]) with engine tests using a Larzac 04 turbofan engine and distortion generators installed upstream from the compressor system to simulate inlet flow distortion. Scheidler et al. [8] enhanced these investigations by means of an active stabilization of a Larzac 04 Low Pressure

Compressor (LPC) while operating with distorted inflow conditions. Rademakers et al. focused on s-duct typical inlet distortions and accordingly generated a variety pure pressure distortion patterns [9] as well as combined pressure-swirl distortion patterns [10]. The influence of these distortion patterns on the performance and stability of the entire inlet-propulsion system was assessed. High fidelity CFD simulations were conducted by Barthmes et al. [11] and Haug et al. [12] to assess the aerodynamic flow condition within a compressor stage in a setup with an upstream installed distortion generator.

Interactions between the flow within the inlet and compressor are neglected if both are considered as isolated systems. These interactions hence need to be included to enlarge knowledge within this field of research and fulfill the increasing requirements of future integrated propulsion systems. The Institute of Jet Propulsion recognized the need of an experimental setup enabling investigations on a full-scale inlet-propulsion system as it is typical for modern Unmanned Combat Aerial Systems (UCAS).

2. General project definition

2.1 Goals

The main goals of the current project were defined prior to the selection of a designated engine inlet system for research. This led to four main requirements for the design of the inlet. The geometry of the inlet system for experimental testing in the ETF should:

1. provide useful data for the validation and optimization of CFD simulations,
2. enable assessment regarding the influence of distorted flow provoked in a UCAS-typical engine inlet system on the performance and stability of the Larzac 04 test vehicle,
3. perform detailed investigations on inlet compressor interactions in an experimental setup with the Larzac 04 test vehicle possible, and
4. be adaptable for future investigations on e.g. flow control and optimization within the engine inlet system.

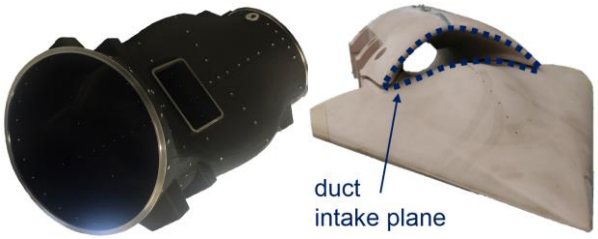

a) bent inlet duct b) generic s-duct

Fig 1. Shaped engine inlet configurations utilized for research at the Institute of Jet Propulsion

Existing engine inlet configurations, which are already available at the Institute of Jet Propulsion for experimental research (i.e. presented by Rademakers et al. [2], [13]), are not suitable to fulfill the previously mentioned project goals as it is explained in the following.

The shape of the “bent inlet duct” (see Fig. 1a and [13]) does not represent an inlet system typical for military applications (see requirement 2). The “generic s-duct” (see Fig. 1b and [2]) has a UCAS-typical geometry, however, only partly covers the compressor face. Hence, there is no all-encompassing fulfillment of requirement 2. The fore body (representing the front part of a UCAS airframe) and the complex shape of the intake plane (see Fig. 1b, indicated in blue) make it furthermore difficult to fulfill requirement 1 because the CFD setup needs to be validated for the simulation of both external and internal flow.

It was hence decided to design a Military Engine Inlet Research Duct (MEIRD) specifically for the planned experimental and numerical investigations within the current research project.

2.2 Project phases

This paper describes the following project phases:

A. Analysis on a baseline s-duct geometry and the establishment of the MEIRD geometry (see Chapter 3).
B. Definition of an instrumentation concept for future research duct with the MEIRD geometry (see Chapter 4).
C. Development of the hardware for experimental testing (see Chapter 5).
D. Manufacturing and installation of all hardware as well as commissioning of the setup (see Chapter 6).

3. Establishment of the MEIRD geometry

The MEIRD geometry was established after an iterative design process supported by CFD simulations. First, a baseline geometry (see Chapter 3.1) was defined and analyzed. Then, 22 modified versions of the baseline geometry were established to assess the influence of local changes of the geometry on the aerodynamics within the inlet system and the distortion patterns at the Duct Outlet Plane (DOP). The flow solver TRACE 8.0 was used for the presented CFD simulations. This software has been developed at the Institute of Propulsion Technology of the German Aerospace Center. The main specifications of all CFD simulations are listed in Tab. 1. The specified outlet static pressure of leads to a mass flow of ca. 26 $^{kg}/_{s}$.

The enlargement of the general understanding of flow phenomena in complex shaped engine inlet systems was the main objective of these investigations. The results contributed to the establishment of an interesting and designated military engine inlet duct for research purposes. It is noted that an optimization of the baseline geometry in terms of flow distortion and total pressure loss was not a main purpose of the presented CFD simulations because of two reasons:

- The provoked distortions within the MEIRD geometry need to be distinct enough to fulfill the project requirements (see Chapter 2.1).
- The shape of the inlet geometry cannot be too complex in order to facilitate both CFD simulations and the manufacturing of the hardware. This improves the comparability between experimental and numerical investigations.

The optimization of an engine inlet geometry can only be conducted sufficiently by using a fully automated process. Such optimizations were already presented by Kächele et al. [5], [6] and will also be part of future research at the Institute of Jet Propulsion.

It is not within the scope of this paper to review the results of all 22 geometry variations in detail. Three main perceptions from these initial CFD investigations are described in Chapter 3.2 until 3.4 because of their major influence on the final shape of the MEIRD geometry (see Chapter 3.5).

number of nodes		ca. 5*M*
numerical boundary conditions	inlet	P_{t0} = *101,325 Pa*
		T_{t0} = *288.15 K*
	outlet	P_s = *85,000 Pa*

Tab. 1. Setup of the CFD simulations

d_{DOP}	*0.454 m*
area ratio (A_{DOP} / A_{DIP})	*1.1739*
offset between DIP & DOP	*1·d*
length (along x-axis)	*3·d*

Tab 2. Baseline s-duct geometry

3.1 Definition of the baseline geometry

The baseline geometry is shown in Fig. 2 and its main geometric properties are listed in Tab. 2. The flow pattern at the DOP of this geometry is shown in Fig. 3a. The diameter of the DOP (d_{DOP} = *0.454 m*) enables the junction of the inlet with a Larzac 04 test vehicle. The area surface ratio (A_{DOP} / A_{DIP} = *1.1739*) is equal to the surface ratio of the engine inlet duct installed in the Alpha Jet aircraft. Noted that the original Alpha Jet power plant consists of two Larzac 04 engines. Both the offset between the Duct Intake Plane (DIP) and DOP (*1·d*) as well as the length of the duct (*3·d*) are best practice values. The properties in Tab. 2 and the position of the center line are equal for all established geometries. This makes it easier to correlate a certain geometry change with a change of the internal flow. It is moreover noted that all inlet geometries are symmetric in the xz-plane. In most cases the geometry was changed in the cross-sections at *s = 0%*, *40%*, and/ or *66%* (see Fig. 2) where *s* indicates the position at the center line of the geometry percentagewise.

3.2 Kidney shape at the DIP

In a first step the shape of the DIP is changed into a kidney shape (baseline mod1). This shape transforms between *s = 0%* and *s = 40%* continuously into an elliptical shape. This modification in the front part of the inlet geometry influences the aerodynamics within the entire inlet system. A counter-rotating twin

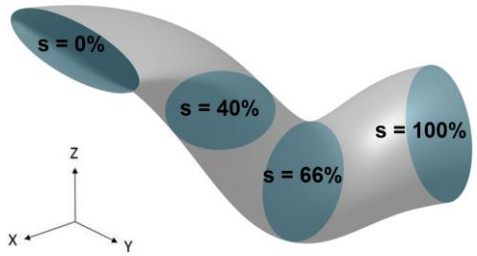

Fig. 2. Baseline s-duct geometry

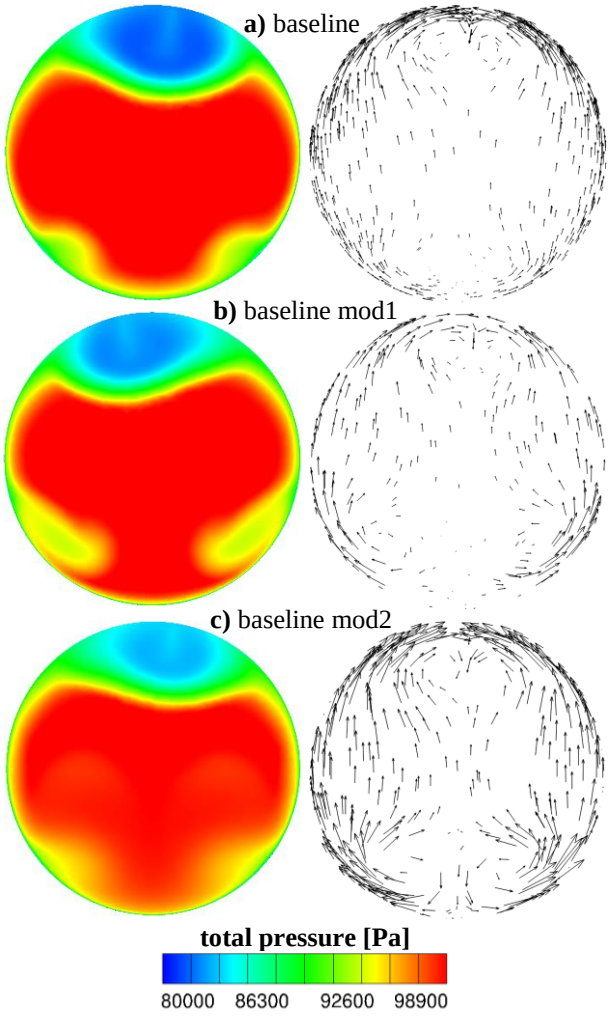

Fig. 3. Total pressure and swirl distortion at the DOP of three different inlet geometries: **a)** baseline geometry, **b)** modified geometry with a kidney shape at the DIP, and **c)** modified geometry with a kidney shaped cross-section between the DIP and *s = 66%*

swirl occurs immediately downstream from the DIP, which is recognizable in the lower part of the distortion patterns at the DOP (see Fig. 3b).

This additional swirl reduces the flow separation at the bottom side of the geometry to a minimum and moreover, causes that an increased part of the mass flow through the inlet is forced upwards. This slightly suppresses the flow separation within the upper part of the inlet geometry downstream from the cross-section at *s = 66%*, which is recognizable by a decreased total pressure distortion in the upper part of the DOP (see Fig. 3b). Moreover, Tab. 3 depicts that both the maximum total pressure loss

$$P_{t,loss,max} = \left(\frac{P_{t0} - P_{t,DOP,max}}{P_{t0}}\right) \cdot 100\% \qquad (1)$$

and the maximum value of the DC60 coefficient

$$DC60_{max} = max\left(\frac{\overline{P_{t,DOP}} - \overline{P_{t,DOP,60°segment}}}{\bar{q}}\right) \qquad (2)$$

at the DOP decrease for the baseline mod1 case.

In a second step, the cross-section *at s = 0%* and *s = 40%* were adapted into a kidney shape (baseline mod2). The shape transforms continuously into an elliptical shape at *s = 66%*. The positive influence of the provoked counter-rotating twin swirl is even better recognizable in this case. This is shown by the distortion pattern plots (see Fig. 3c) as well as the evaluated distortion coefficients (see Tab. 3).

It is noted that the surface area of all cross-sections was kept constant while changing the shape of the cross-section. The kidney shape in the front part of the inlet system is thus advantageous from an aerodynamic point of view. It was hence decided to include this feature within the MEIRD geometry. It should, however, be taken into account that the coverage of the compressor plane can be reduced due to this particular shape in the front part of an inlet system.

	$P_{t,loss,max}$	$DC60_{max}$
baseline	*22.27%*	*0.433*
baseline mod1	*21.60%*	*0.369*
baseline mod2	*21.18%*	*0.319*

Tab 3. Distortion coefficients for the flow at the DOP of three inlet geometries

3.3 Rectangular shape at *s=66%* of the geometry

The shape of the cross-section at *s = 66%* was investigated in detail. In the following only two local modifications are compared. In the first place this cross-section has sharper edges within the upper part (baseline mod3, see Fig. 4a) and secondly, sharper edges within the lower part

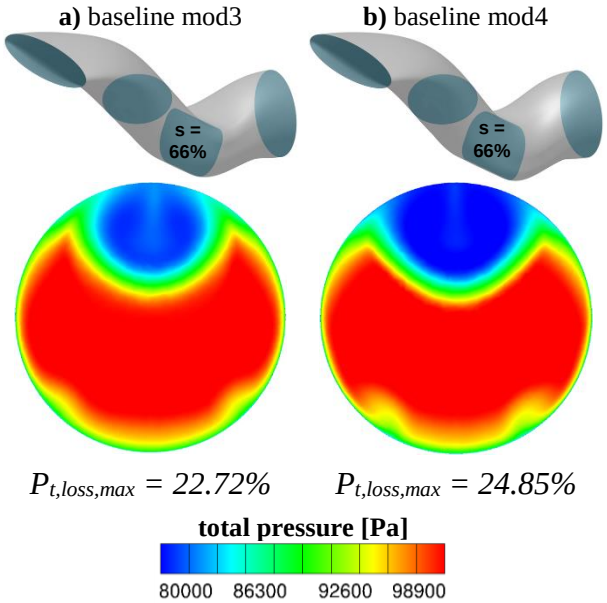

Fig 4. Total pressure distortion pattern for **a)** baseline mod3 and **b)** baseline mod4

(baseline mod4, see Fig. 4b). In both cases the surface area and the position of the cross-section is equal in such way that the inlet geometry upstream from *s = 66%* is similar. Hence, the changing flow conditions in the duct (e.g. the flow separation) are provoked solely by the different shapes at *s = 66%*.

Figure 4 also shows the pressure distortion patterns at the DOP for both cases. For baseline mod3 the larger radii in the lower part of the cross-section (see Fig. 4a) lead to shift of the mass flow distribution towards the upper part of the inlet, which has a stabilizing effect on the flow separation. A weaker flow separation occurs, which is identified by a decreased loss of total pressure at the DOP compared to baseline mod4 (see Fig. 4b).

It was chosen for the MEIRD geometry to decrease the radii of the cross-section at ca. *s = 72%* of the s-duct as much as possible. This specific cross-section was chosen since it is parallel to the yz-plane. The extent in vertical direction was moreover reduced, which leads to a wider cross-section in order to force the mass flow towards the region with flow separation.

3.4. Diffusing character of the geometry

For all previously described cases the cross-sectional area increases constantly from $A = 0.1379\ m^2$ at the DIP up to $A = 0.1619\ m^2$ at

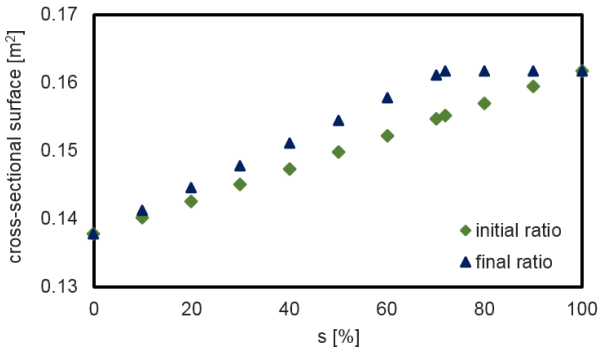

Fig 5. Variation of cross-sectional surface along the center line

the DOP as it is displayed in Fig. 5 (depicted in green). It was shown by e.g. Kächele et al. [6], and also by Siller and Voss [14] that a variation of the cross-sectional area along the centerline generally has a major influence on the distortion and pressure loss within an inlet system. It is advantageous to create a sort of settling chamber upstream from the DOP, which enables the distortion to mix out. It was nevertheless chosen to keep the gradient of the cross-sectional area along the centerline relatively simple in order to ease the assessment of aerodynamic phenomena in relation with the geometry of the duct by means of experimental and numerical data.

For the MEIRD geometry the cross-sectional area along the center line increases linearly between the DIP and *s = 72%* from $A = 0.1379\ m^2$ up to $A = 0.1619\ m^2$ and is then kept constant between *s = 72%* and the DOP. This is depicted in Fig. 5 in blue.

3.5 The MEIRD geometry

Ten cross-sections and a side view of the final MEIRD geometry are displayed in Fig. 6. The total pressure and swirl distortion patterns, which are provoked by this geometry at the DOP are shown in Fig. 7a and Fig. 7b, respectively.

A set of additional design criteria was defined for the final definition of the MEIRD geometry in comparison to the inlet geometries for the preliminary CFD simulations presented in the first part of this chapter. In the following two subchapters it is distinguished between aerodynamic and geometric design criteria.

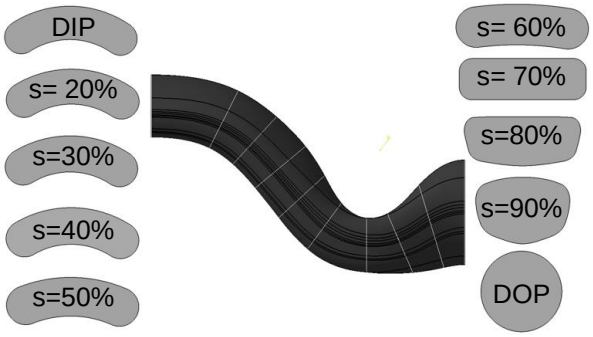

Fig 6. Ten cross-sections of the MEIRD geometry along the center line

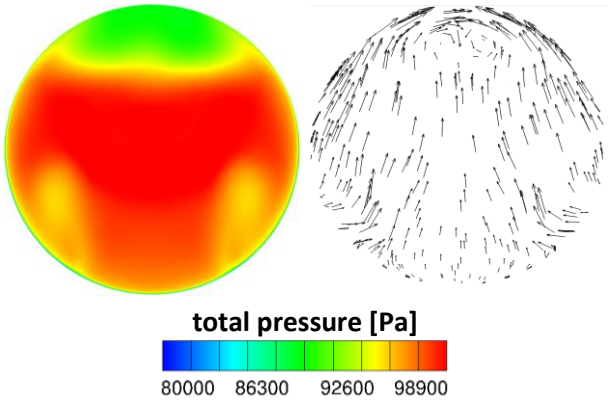

Fig 7. Total pressure and swirl distortion pattern at the DOP of the MEIRD geometry

3.5.1 Aerodynamic design criteria

Four aerodynamic constraints were defined for the establishment of the MEIRD geometry. The flow within the entire inlet system should be subsonic ($Ma < 1$) and the distortion at the DOP should be such that $DC60_{max} < 0.7$ to ensure a safe operation of the inlet system in a setup with the modified Larzac 04 C5 test vehicle. Furthermore, constraints for the flow properties at the DOP are necessary because of the intended measurement equipment. The utilized five-hole probes are designed and calibrated for a flow with $Ma < 0.6$ and maximal flow angles of $\Theta < 24°$.

3.5.2 Geometric design criteria

The experimental setup is schematically shown in Fig. 8. It is noted that the flow does not enter the test section horizontally due to the particular design of the facility. The available space in the existing setup was taken into account for the shape of the inlet in such way that it can also be installed upside-down in front of the test vehicle. This means that it is rotated with $180°$ around its x-axis. This enables experimental investigations of the duct with different aerodynamic conditions at the DIP due to the angled inflow in the test section of the ETF.

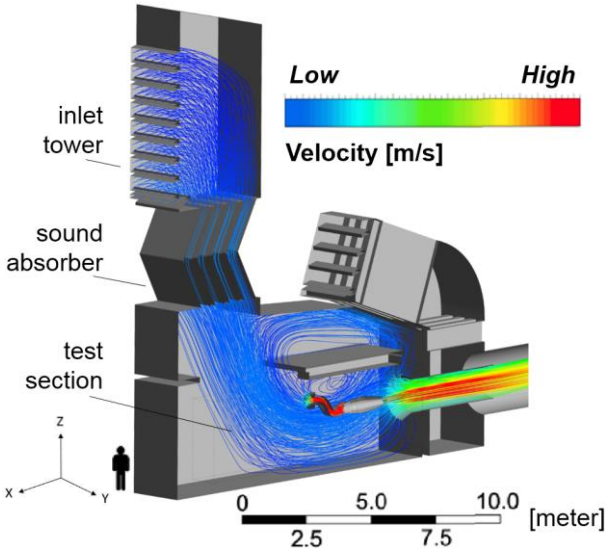

Fig 8. CFD simulation of the MEIRD geometry installed in the ETF with the modified Larzac 04 test vehicle

A bellmouth-like intake lip was designed to enable a homogeneous guidance of the flow from the test section into the MEIRD. The design of the intake lip was supported with the help of CFD simulations (see Fig. 9).

Finally, the MEIRD geometry fully covers the compressor face. It is noted that the shape of the intake lip was not considered while proving the coverage of the compressor face since the intake lip is not directly part of the MEIRD geometry itself.

4. Definition of instrumentation for experiments

An instrumentation of the MEIRD for experimental research is essential for the fulfillment of the project goals defined in Chapter 2.1. Three different types of aluminum adapters (see Chapter 4.1 – 4.3) were integrated within the carbon fiber structure to enable the installation of additional hardware (i.e. mainly sensors and probes). These adapters all have a flange to enable a secure integration of the adapters between different layers of carbon fiber. Additional measurement instrumentation being installed downstream from the duct, within the engine, and the rest of the test bed is

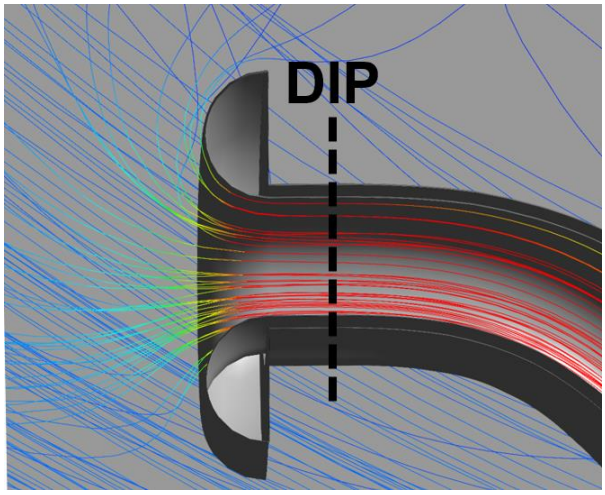

Fig 9. CFD simulation of the flow entering the MEIRD through the intake lip

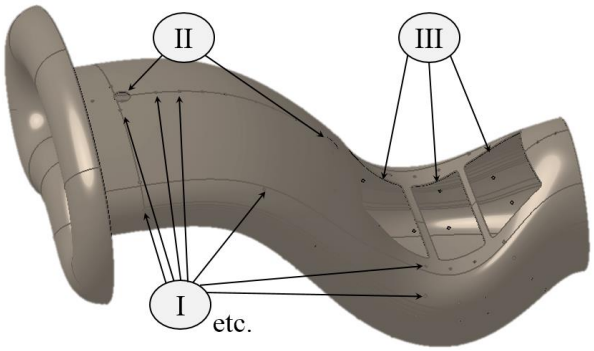

Fig 10. The MEIRD geometry including the positions of the foreseen instrumentation

overviewed in Chapter 4.4. A designated system utilized for data acquisition is described in Chapter 4.5.

4.1 Static pressure taps

Altogether 143 adapters were integrated for the installation of wall static pressure sensors (see Fig. 10, Pos. I). In total 24 of those adapters were positioned along the upper and lower wall at the symmetry plane of the inlet (ten adapters at the top side and 14 adapters at the bottom side). The remaining 119 adapters are spread over ten different cross sections. The latter adapters are especially positioned at the bottom side of the duct within several regions where flow separation occurs according to CFD simulations. Figure 11a depicts the region where the local value of skin friction approaches zero in blue. This generally is an indicator for flow separation and thus of particular interest for the positioning of static pressure taps.

4.2 Boundary layer probes

Two adapters were integrated at the upper side of the wall at the symmetry plane (see Fig. 10, Pos. II). These adapters will mainly be used for the installation of boundary layer probes. The first adapter is positioned at the DIP and the second adapter is positioned at $s = 40\%$. These positions were selected because of two reasons. First, the boundary layer probes are not designed to measure flow conditions with large flow angles. The swirl is expected to be relatively moderate in the front part of the MEIRD geometry, especially at the upper side of the cross-sections due to moderate local geometry changes. Second, the development of the boundary layer thickness along the upper side of the inlet can be determined in this way since the adapters are positioned at the same circumferential position. This is interesting for the validation and optimization of CFD simulations.

4.3 Opening near flow separation

A large scale flow separation is expected to occur within the upper part of the geometry. It was decided to integrate three openings in this part of the MEIRD to increase the possibilities for detailed flow measurements. The location of flow separation was determined with the help of CFD simulations. The blue region in Fig. 11b again indicates the region where the skin friction is extremely low and hence CFD expects the flow to detach. Both the position and the extension of this region do not change significantly over the operating range of the test vehicle.

4.4 Further engine and test bed measurement instrumentation

4.4.1 Measurement instrumentation at the AIP

The MEIRD can directly be installed in front of the test vehicle to provoke the maximal amount of interaction between the flow in the inlet and the compressor system. Nevertheless, it is also of interest to determine the flow condition between the MEIRD's outlet plane and the compressor face for the setup and validation of CFD simulations. With Aerodynamic Interface Plane (AIP) it is referred to this measurement

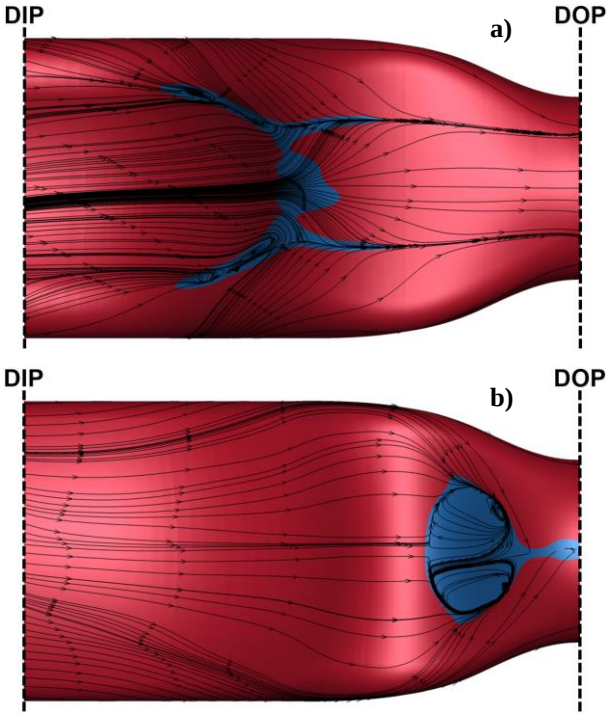

Fig 11. Regions with expected flow separation at the **a)** bottom side and **b)** upper side of the MEIRD

plane since it is not necessarily equal to the DOP. A measurement rake was specifically designed for this purpose. It is installed in a housing, which can be displaced in circumferential direction to measure the aerodynamic flow condition at a large number of positions. In total 18 probes are available for the installation in the measurement rake. Ten five-hole probes are used to measure three dimensional flow properties. Furthermore, six standard pitot probes are available for further pressure measurements with low sampling rates ($f_s \leq$ 1kHz) and two pitot probes with an integrated Kulite®-transducer for pressure measurements with sampling rates up to (f_s = *100kHz*).

4.4.2 Engine instrumentation

The available Larzac 04 turbofan engine is extensively equipped with measurement instrumentation. Experimentally obtained data can hence not be compared with original engine specifications and thus it is simply referred to this modified Larzac 04 engine as "test vehicle". Especially the instrumentation in the LPC is important for the fulfillment of the current project goals and thus briefly summarized in the following.

The unsteady flow behavior at the intake plane of the engine is assessed with five dynamic pressure transducers, which are installed *10 mm* upstream from the first fan stage at equally spaced circumferential positions in the casing of the LPC. In addition, an array with nine dynamic pressure transducers is installed in the casing over the first fan stage.

The development of a flow distortion through the LPC is determined by using pitot probes within three vanes of the first stator stage and pitot probes within two vanes of the first row of the second tandem stator. A single rake with six pitot probes is installed behind the second row of the second tandem stator to determine the total pressure at the exit of the LPC.

4.4.3 Test bed instrumentation

Pressure and temperature is measured at several positions within the ETF to set up the boundary conditions of CFD simulations. The relative humidity is measured at a metrological office, which is located at the same university campus as the Institute of Jet Propulsion.

4.5 Data acquisition

Two state of the art data acquisition systems are used in parallel during testing campaigns in the ETF. Stößel and Niehuis [15] describe the primary data acquisition system based on National Instruments (NI) PXIe hardware and NI LabVIEW software, which was established for an overall monitoring of the test bed and the jet engine during operation. This system can be utilized for different jet engines being operated in the ETF.

The secondary data acquisition system is based on NI cRIO (Compact Real-Time In-/ Output Controller) hardware and NI LabVIEW software. This system can specifically be programmed according to the goals of a certain testing campaign as it is described by Rademakers et al. [16]. The current system is used for pressure, vibration, strain gauge, and temperature measurements. The hardware is also highly adaptable to the experimental setup due to the usage of multiple NI9144 extension chassis. These chassis can be installed anywhere in the ETF and thus also directly next to the

inlet and compressor system such that the length of the tubes for pressure measurements can be reduced to a minimum. This also reduces the pneumatic damping within the tubes allowing reasonable pressure measurements at high sampling rates.

The setup for the investigations on the MEIRD solely consists of almost 300 pressure probes and taps (standard instrumentation of the test vehicle not included). It was hence a main focus during the programming of the secondary data acquisition system to enable a large amount of pressure measurements simultaneously. Currently, the system can simultaneously sample up to 240 pressure values with a maximal sampling rate of *1 kHz* per channel.

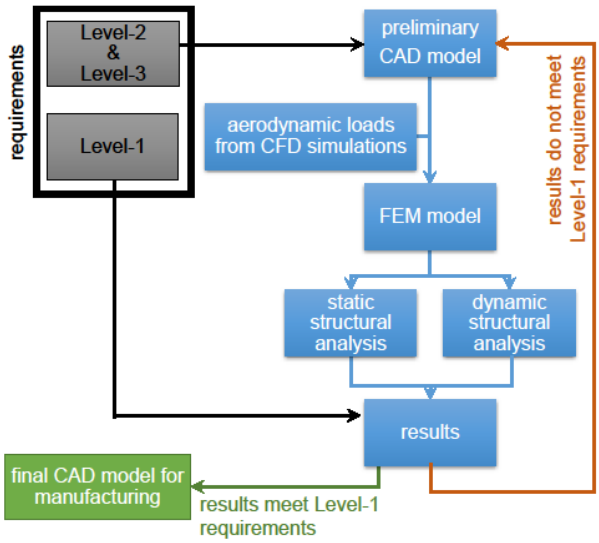

Fig 12. MEIRD development procedure

5. Development of the MEIRD

This chapter describes the project phase in which the MEIRD geometry (see Chapter 3.5) and the defined measurement instrumentation (see Chapter 4.1 – 4.3) were developed into a Computer-Aided Design (CAD) model for the manufacturing of the actual hardware. The MEIRD will be utilized for testing in the institute's ETF and thus, in addition, four side mountings for the installation in the ETF and an adapter for the junction with the test vehicle had to be integrated within the CAD model of the MEIRD. With "the duct" it is in the following referred to the MEIRD as it will be installed in the ETF. Figure 12 shows a schematic representation of the applied development procedure. During the development it was distinguished between Level-1, Level-2, and Level-3 requirements.

A safe operation of the engine and the duct in the ETF is ensured by means of the Level-1 requirements. First, the strength of the duct's structure needs to be sufficient for all possible operating conditions in the ETF. Second, an excitation of the duct's eigenmodes during operation must be avoided.

The Level-2 requirements allow the feasibility of the duct's manufacturing within a certain financial framework. Especially the choice of the materials and the defined manufacturing accuracy have a major influence on both the feasibility and the costs. The respective restrictions differ for each component of the duct and are hence not defined explicitly for the sake of convenience.

By satisfying all Level-3 requirements it is ensured that the experimental setup will provide high quality experimental data for the fulfillment of the four main project goals as defined in Chapter 2.1. Main examples of Level-3 requirements are e.g. the positioning of measurement instrumentation and once again the manufacturing accuracy of the duct and all integrated components. A sufficient stiffness of the duct should furthermore ensure a minimal deformation of the structure caused by aerodynamic forces during operation.

In a first step a CAD model was made by taking the Level-2 and Level-3 requirements into account. Then, a Finite Element Method (FEM) model, including the aerodynamic loads resulting from CFD simulations, was established. The results of both static and dynamic structural analyses were then compared with the Level-1 requirements. Several iterations were necessary to develop a duct model, which fulfilled all Level-1, Level-2, and Level-3 requirements. Selected results from the final development iteration are shown in the following subsections.

5.1 Establishment of a CAD model

In total 152 components were integrated in the duct's structure to enable both the installation of

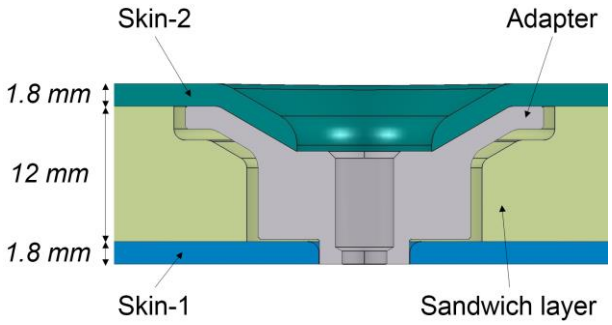

Fig 13. Integrated adapter for the installation of wall static pressure sensors

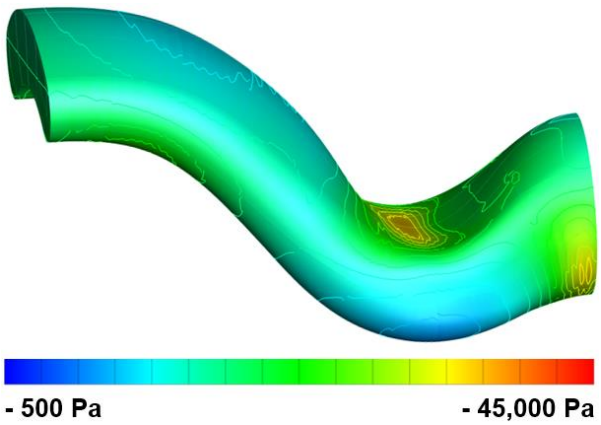

Fig 14. Aerodynamic loads on the duct's structure predicted for the test vehicle at its full thrust setting

measurement equipment within the duct as well as the installation of the duct in the ETF. This was a main challenge during the development of the duct. All components had to be integrated while ensuring a high manufacturing accuracy and a high stiffness of the structure at the same time. It was hence decided to build up the structure in three layers as it is schematically shown in Fig. 13.

For the middle layer it was chosen for an aluminum sandwich structure because of the following advantages. The stiffness of the entire structure increases significantly, which leads to large reduction of local deformations caused by aerodynamic loads during operation. At the same time the thickness of both carbon fiber layer (Skin-1 and Skin-2) can be reduced, which eases the manufacturing. The conventional wet layup technique was chosen for the manufacturing of the main part of the structure.

It is noted that the sandwich structure is not foreseen within specific parts of the duct. The complex shape of the intake lip and the side mountings at both sides of the duct makes the integration of a sandwich structure almost impossible. For the intake lip it is sufficient to solely use two *1.8 mm* layers of carbon fibers since the aerodynamic forces are small and possible deformations would not influence the aerodynamic conditions within the duct. The four side mountings are specifically designed while considering that a sandwich structure cannot be integrated. It was hence decided to manufacture the side mountings with pre-impregnated composite fibers by using the out of autoclave manufacturing process, which is characterized by a high manufacturing precision.

5.2 Aerodynamic loads as input data for structural analyses

The aerodynamic loads on the duct were predicted with the help of CFD simulations. It was found that the patterns of these loads over the surface of the duct do not change depending on the operating point of the test vehicle. Only the load levels decrease for reduced operating points. It was hence decided to conduct both static and dynamic numerical structural analyses while considering the full thrust setting of the test vehicle (see Fig. 14).

5.3 Static structural analysis

5.3.1 Stiffness

The carbon fiber structure deforms in a certain extent due to the aerodynamic loads depending on the operating point of the test vehicle. It is not reasonable to adapt the mesh for CFD simulations to such deformations. It was hence defined as Level-3 requirement that a local deformation of the structure is limited to *1 mm* in order to ensure the comparability between experimental and numerical results.

The integration of the aluminum sandwich structure as described in Chapter 5.1 is the main reason for a formidable stiffness of the structure. The maximum locally occurring absolute deformation of the structure was predicted by means of an FEM simulation to be *0.81 mm*. This deformation occurs within the intake lip (see Fig. 15) where the aluminum sandwich structure is not integrated. The maximal deformation in the main part of the duct is predicted to be less than *0.70 mm*.

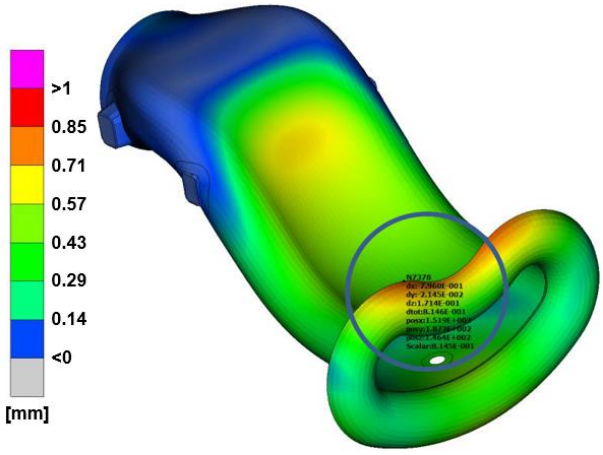

Fig 15. Deformation of the structure as it results from a static FEM simulation

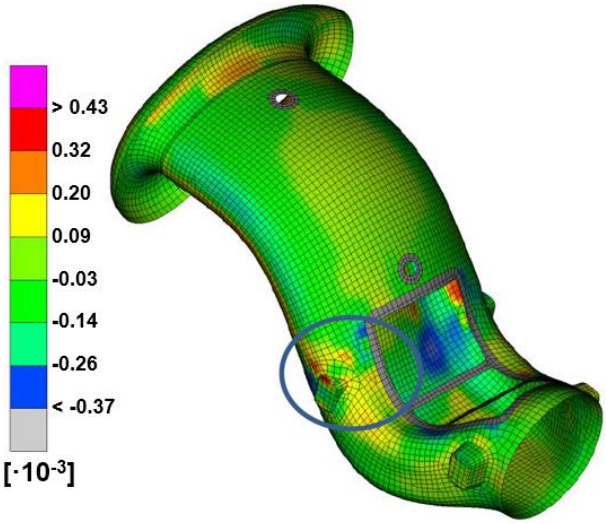

Fig 16. Strain within the structure as it results from a static FEM simulation

5.3.2 Strength

The maximal tolerable strain within the carbon fiber structure for static loads was defined to be $\varepsilon_{limit} = 0.01$. It was not necessary to optimize the model with respect to strength since the respective requirements are negligibly minor in comparison with the stiffness requirements. The most significant strain occurs in the front side mountings (see Fig. 16). Nevertheless, a strength safety margin

$$S = \frac{\varepsilon_{limit}}{\varepsilon_{max}} \qquad (3)$$

of $S > 23$ for the entire structure ensures a safe operation at the ETF.

5.4 Dynamic structural analysis

Dynamic structural analyses were conducted to determine the eigenmodes of the structure. The frequencies of the eigenmodes were then compared with possible sources, which could excite the respective eigenmodes leading to a hazardous vibrational response of the structure. In the following the Blade Passing Frequency (BPF, i.e. the 23rd engine order) of the LPC's first stage was considered.

It is again sufficient to determine the eigenmodes for a single operating point of the test vehicle. Geometrical changes of the duct over the operating range of the test vehicle can be neglected due to the stringent requirements on structural stiffness (see Chapter 5.3.1).

Most distinctive flow phenomena will propagate upstream from the first stage of the LPC with its BPF. The eigenmodes of the duct's structure are compared with the BPF over the entire operating range in Fig 17. Rotating stall can theoretically occur in the entire operating range of the LPC. Such phenomena typically occur with a frequency of at least *50%* of the BPF, which is correspondingly indicated with a red area in Fig. 17. The first 40 eigenmodes of the duct's structure vary between *58 Hz* and *737 Hz* as it is depicted in blue (see Fig. 17). The eigenmodes do not intersect with the BPF nor typical unsteady flow phenomena, which can be provoked due to transonic operating conditions within the LPC.

The main motion of the structure in the unlikely event of a modal excitation while considering the first three eigenmodes would occur in the front part of the system. It was hence decided to install a tri-axial accelerometer to monitor vibrations in this part of the structure to fully ensure a safe operation during testing campaigns.

6. Manufacturing and integration

All parts for the experimental setup are manufactured and currently being integrated within the ETF. The first experimental investigations will be conducted by the end of the year 2016 and results will be presented in future publications.

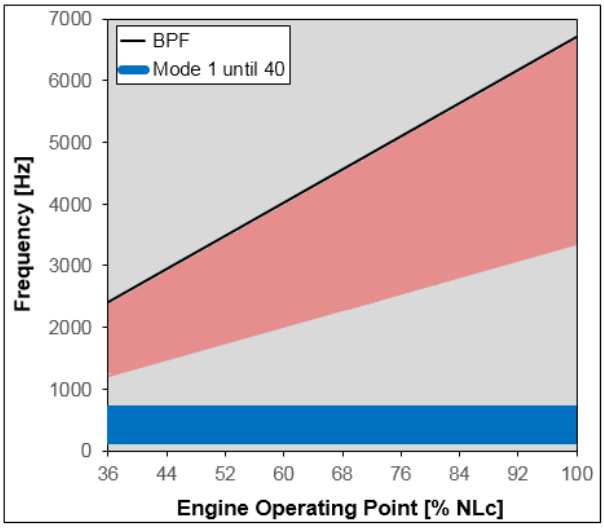

Fig 17. Comparison of the first 40 eigenfrequencies of the duct's structure with the BPF of the LPC's first stage

7. Conclusion and outlook

The geometry of a typical military engine inlet system for research purposes was designed with the help of CFD simulations (Goal 2). The geometry was designed for both numerical and experimental investigations. Because of that reason the geometry does not include complex shapes such as sharp edges to ensure an optimal comparability between experimentally and numerically obtained data. The development process for the establishment of the actual hardware for experimental testing was summarized.

The instrumentation concept for the entire experimental setup was of particular importance in order to gain a sufficient dataset for the validation and optimization of CFD simulations (Goal 1). The same measurement instrumentation enables investigations on inlet-compressor interactions (Goal 3).

Adapters for large exchangeable inserts were furthermore integrated in the duct's structure within the region where a large scale flow separation is expected to occur. These exchangeable inserts enables the installation of extensive measurement instrumentation to contribute to the fulfillment of both Goal 1 and Goal 3. Such inserts moreover enable the installation of devices for investigations on passive and active flow stabilization in s-duct engine inlet systems (Goal 4).

Nomenclature

Symbols

A	cross-sectional surface [m^2]
d	diameter [m]
$DC60_{max}$	60°-segment distortion coefficient [-]
f_s	sampling rate [kHz]
Ma	Mach number [-]
NLc	corrected spool speed of the LPC [%]
P_s	static pressure [Pa]
P_{t0}	ambient total pressure [Pa]
$P_{t,loss,max}$	total pressure loss [%]
s	position at the center line [%]
S	safety factor [-]
T_{t0}	ambient total temperature [K]
ε	strain [-]

Abbreviations

AIP	Aerodynamic Interface Plane
BPF	Blade Passing Frequency
CAD	Computer-Aided Design
CFD	Computational Fluid Dynamics
DIP	Duct Intake Plane
DOP	Duct Outlet Plane
ETF	Engine Test Facility
FEM	Finite Element Method
MEIRD	Military Engine Inlet Research Duct
NI	National Instruments
LPC	Low Pressure Compressor
UCAS	Unmanned Combat Aerial System

References

[1] Muth, B., Bindl, S., Lehmann, C., Niehuis, R., "Numerical Investigation of Inlet Induced Distortions of a Turbofan Engine Within an Indoor Test Facility", AIAA-2009-4826, In Proceedings of the 45th AIAA/ASME/SAE/ASEE Joint Propulsion Conference & Exhibit, Denver, Colorado, USA, August 2009.

[2] Rademakers, R.P.M., Bindl, S., Brehm, S., Muth, B., and Niehuis, R., "Investigation of Flow Distortion in an Integrated Inlet of a Jet Engine", DLRK2013-301349, In Proceedings of the 20th German Aerospace, Stuttgart, Germany, September 2013.

[3] Brehm, S., Kächele, T., and Niehuis, R., "CFD Based Comparison of the Aerodynamics within S-Duct Inlet Configurations at Sub- and Full-Scale Engine Test Facilities", ISABE-2015-20021, In Proceedings of the 22nd International Symposium on Air Breathing Engines, Phoenix, AZ, USA, October 2015.

[4] Brehm, S., Kächele, T., and Niehuis, R., "CFD Investigations on the Influence of varying Inflow Conditions on the Aerodynamics in an S-Shaped Inlet Duct", AIAA-2014-3595, In Proceedings of the 50th AIAA/ASME/SAE/ASEE Joint Propulsion Conference & Exhibit, Cleveland, USA, June 2014.

[5] Kächele, T., Brehm, S., and Niehuis, R., "Parametric CFD Study on Performance of Double-S-Shaped Ducts with Varying Cross Sectional Shapes", ISAIF12-037, In Proceedings of the 12th ISAIF, Lerici, Italy, July 2015.

[6] Kächele, T., Brehm, S., and Niehuis, R., "Numerical Parameter Study on Influences of Geometry Modifications on Performance of Double-S-Shaped Ducts", ISABE-2015-20022, In Proceedings of the 22nd International Symposium on Air Breathing Engines, Phoenix, AZ, USA, October 2015.

[7] Schmid, N. R., Leinhos, D. C., and Fottner, L., "Steady Performance Measurements of a Turbofan Engine With Inlet Distortions Containing Co- and Counter-Rotating Swirl From an Intake Diffuser for Hypersonic Flight", In *ASME J. Turbomach.* 123(2), pp. 379–385, 2001.

[8] Scheidler, S. and Fottner, L., "Operational Characteristics of a Twin-spool Turbofan Engine at Inlet Distortions with Reduced Surge Margin", RTO-AVT-2003-029, In Proceedings of the RTO-AVT-100 Symposium, Warsaw, Poland, October 2003.

[9] Rademakers, R.P.M., Bindl, S., and Niehuis, R., "Effects of Flow Distortions as They Occur in S-duct Inlets on the Performance and Stability of a Jet Engine", In *ASME J. Eng. Gas Turbines Power* 138(2), February 2016.

[10] Rademakers, R.P.M., Bindl, S., and Niehuis, R., "Influence of Secondary Flow within Integrated Engine Inlets on the Performance and Stability of a Jet Engine", ISABE-2015-22148, In Proceedings of the 22nd International Symposium on Air Breathing Engines, Phoenix, AZ, USA, October 2015.

[11] Barthmes, S., Haug, J.P., Lesser, A., and Niehuis, R., "Unsteady CFD Simulation of Transonic Axial Compressor Stages with Distorted Inflow", In *Advances in Simulation of Wing and Nacelle Stall*, Eds. Radespiel, R. et al., Vol. 131 of *Notes on Numerical Fluid Mechanics and Multidisciplinary Design*, Springer, pp. 303–321, 2015.

[12] Haug, J.P., Barthmes, S., and Niehuis, R., "Full Annulus Unsteady CFD Simulations on Effects of Inflow Distortions in a Transonic Axial Compressor Stage", IGTC-2015-0090, In Proceedings of the 11th International Gas Turbine Congress, Tokyo, Japan, November 2015.

[13] Rademakers, R.P.M., Kächele, T., and Niehuis, R., "Integration of a Highly Bent Engine Inlet in an Engine Test Facility", ISROMAC-2016-112, In Proceedings of the 16th International Symposium on Transport Phenomena and Dynamics of Rotating Machinery, Honolulu, HI, USA, April 2016.

[14] Siller, U. and Voss, C., "Automated Optimization of a Double S-Shaped Inlet for Minimum Loss and Reduced Sight onto the Engine Face", ISROMAC13-TS32, In Proceedings of the 13th International Symposium on Transport Phenomena and Dynamics of Rotating Machinery, Honolulu, HI, USA, April 2010.

[15] Stößel, M., Niehuis, R., "Einrichtung einer Messdatenerfassungsanlage mit Online-Datenservereigenschaften mittels NI PXI und LabVIEW Real-Time", In *Virtuelle Instrumente in der Praxis 2010*, Eds. Jamal, R. and Heinze, R., VDE Verlag, ISBN 978-3-8007-3235-7, pp. 25-29, 2010.

[16] Rademakers, R.P.M., Pohl, A., Niehuis, R., "Hochfrequente Mehrkanal Druckmessungen an einer Triebwerkversuchsanlage", In *Virtuelle Instrumente in der Praxis 2015*, Eds. Jamal, R. and Heinze, R., VDE Verlag, ISBN 978-3-8007-3669-0, pp.75-78, 2015.

Copyright Statement